Complex mechanical response of stomatocyte morphology: Implications for the nuclear envelope.

Beatrice J. Geiger and Weria Pezeshkian*
Niels Bohr International Academy, Niels Bohr Institute, University of Copenhagen, Copenhagen, Denmark.
*Corresponding author: weria.pezeshkian@nbi.ku.dk

Abstract
Among the fascinating shapes that biomembranes exhibit are stomatocytes, found for example in nuclear membranes and open autophagosomes. These morphologies, characterised by a high topological genus, can be visualised as spherical double membranes connected by neck-like structures. The necks are often occupied by specific biomolecular complexes, such as the nuclear pore complex, which divide the space into three distinct compartments. Understanding how the size of these necks responds to pressure gradients is fundamentally important for unravelling the influence of mechanical stimuli on traffic control through the necks, for example, in nuclear mechanosensing. In this work, we use computer simulations and theoretical analysis to investigate how neck size responds to variations in pressure or tension. Our findings reveal a two-phase behaviour: below a certain threshold, necks constrict as the pressure gradient increases, while above that threshold, they dilate. This response stems from the pure membrane's mechanics and depends on the magnitude of the pressure gradient, the initial diameter of the neck and the membrane bending rigidity. We also provide a simple equation that links the threshold tension, the neck diameter and the bending rigidity, offering a useful tool to quickly assess different scenarios. Our results furthermore show that protein complexes in the neck partially counteract both constriction and dilation, stabilising neck size while preserving the same two-phase response to membrane tension. These findings uncover a novel, previously overlooked membrane property with implications for organelle shape and function.

INTRODUCTION

Biological and synthetic membranes assume a variety of shapes that are crucial for cell functioning. An interesting example of these is the stomatocyte shape, a concave inward structure resembling a bowl, often with tight openings. From a biomedical point of view, stomatocytes can be an indication of disease. For instance, stomatocytosis, a hereditary or acquired (alcoholism, certain drugs) red blood cell disorder is associated with a stomatocytic shape of the red blood cells [1]. Stomatocyte morphologies are commonly observed under certain physical conditions. For instance, a spherical vesicle with a large surface-to-volume ratio or high osmotic pressure can undergo transitions into a stomatocyte shape [2,3]. This can also be achieved through negative spontaneous curvature [4]. In membranes with high topological genera, stomatocyte structures can form with multiple openings (**Fig. 1b,** Supplementary Fig. 1a) [5–8]. The number of openings equals the surface's topological genus plus one (g+1). Once an opening narrows (from here on referred to as membrane necks) specific molecular machinery can assemble to render the neck impermeable to selected biomolecules, effectively dividing the space into three compartments (see also **Fig. 1a**) [4,9]. Similar structures are observed in cellular membranes, such as autophagosomes and the nuclear envelope [10–16]. In case of the nuclear envelope, for example, the nuclear pore complex effectively regulates biomolecular trafficking through the neck [17–21]. Because of the many potential implications on organelle shape and cell function, it is therefore essential to understand how the size of these necks is regulated in response to common external stimuli and macroscopic parameters, such as osmotic pressure.

An excellent experimental platform for exploring stomatocyte morphology in cellular context is the nuclear envelope (NE). While the NE is a highly complex system, with encapsulated DNA and intermediate filaments within the nucleus also exerting pressure on it [22–26], it is generally accepted that the dominant pressure within the nucleus and cytoplasm arises from the osmotic pressure of proteins and RNA molecules localised to these compartments rather than from chromatin or its associated ions [25,27,28]. Experimental studies of the NE largely agree that increased tension on the nuclear membrane leads to an increase in the diameter of the intact nuclear pore complex (NPC), effectively dilating the nuclear pores [29–33]. In these experiments, tension has been varied through change in osmotic pressure or energy depletion [29,33], by considering different states of cell differentiation [30] or by comparing purified NPCs with those in the native cellular context [31,32]. At lower NE tension a constricted state has been found [29–31]. It is commonly considered that this NPC constricted state is a ground state, from which it then dilates under increased NE tension. However, Taniguchi et al. [30] showed that in cells with structurally impaired NPCs, increase in NE tension led to NPC constriction relative to states of smaller tension. This unexpected opposite behaviour was explained as arising either from the inability of the nuclear membrane to properly transfer forces to defective NPCs or from tension being already alleviated by an overdilation of some NPCs [30]. To add to this contradicting behaviour, a molecular dynamics simulation of the NPC in a membrane neck

also showed that NPC diameter could be maintained under tension, in addition to the expected tension-driven dilation [32].

Since the NPC is a complex biomolecular aggregate [34,35] the above diverse behaviour could arise from its intricate mechanics and mechanosensitivity. In this work, however, we provide an alternative possibility, namely that the complex mechanical response of the membrane in the associated morphology could account for the two-sided responses to membrane tension. For this, we perform mesoscopic simulations of biomembranes together with theoretical analyses to shed light on the response of membrane necks. First, we explore a simple membrane for a more general approach and attain results transferable to any such membrane system. We then add complexity by incorporating a protein complex, addressing the discussed discrepancies and elucidating the role of the NE membrane in nuclear mechanosensing. Our findings suggest a previously overlooked material property of membranes to be of central relevance for understanding the characteristic response to mechanical stress of these membrane systems, which are at the heart of sub-cellular structure.

RESULTS

1. Stomatocyte forms easily, especially for surfaces with high topological genus

We first obtained an overview of conditions in which a stomatocyte morphology forms over a wide range of topological genera, from the well-understood spherical case (genus 0) up to a genus of 20. **Fig. 1b** shows a summary of exemplary membrane configurations for different genera for a reduced volume of $v = 0.3$ in good agreement with the previous studies [7]. Indeed, similar results were obtained for $v < 0.45$ or a negative spontaneous curvature (results not shown). For high-genus surfaces (g = 18-20), spherical stomatocytes also formed without the need for any volume constraint or negative spontaneous curvature. This may be due to the mixing entropy contributions of the necks, as at low temperatures (or high bending rigidity), the necks concentrate around a disc that divides the inner space into two compartments (Supplementary Fig. 1b). For surfaces with smaller topological genus (fewer necks), the necks tend to concentrate in a specific region of the vesicle (see Supplementary Fig. 1a).

2. Stomatocyte necks first constrict, then dilate under internal pressure

We then selected one of the structures with g = 20 from the previous section to investigate its response to an increase in internal pressure, which manifests as an increase in lateral tension on the membrane [29,36,37]. In the simulation, achieving this is challenging because the volume of the internal compartment (Compt. I in **Fig. 1a**) cannot be precisely measured, unlike the internal volume of a triangulated surface (Compt. II in **Fig. 1a**). Instead, we simulated the stomatocyte containing a large bead. During the simulation, this core bead is gradually

expanded, representing a slow and continuous increase in the volume of the inner compartment I, analogous to the effects of internal pressure increase. The simulations were performed at near constant surface area by coupling to a harmonic stretching potential ($K_A = 1000\ \mathrm{k_B T}$) for three different membrane bending rigidities of $\kappa = 5, 10, 20 k_B T$ (see Methods for more detail and Supplementary Fig. 2 for more results). Additionally, we examined the same system decorated by 5% directional curvature-inducing proteins, which assemble in the necks; this configuration was previously used as a minimal mesoscopic model for nuclear membranes [5]. For defined core bead sizes, we subsequently performed constant bead size simulations to obtain higher sampling and exclude the effect of the rate of bead radius increase.

In all simulations, with and without protein assemblies, the results show that increasing the core bead radius first leads to a constriction of all necks after which dilation of some necks occurs (Supplementary Fig. 2). **Fig. 1c** shows the results after additional constant bead size simulations for $\kappa = 10\ k_B T$. The constrictive response can be quantified in the neck diameter (D_p) distribution as diameters move from larger values at rescaled core radius $\bar{r}_{core} (= r_{core}/r_{syst}) = 0.48$ to very small values at $\bar{r}_{core} = 0.83$. Protein assemblies in the necks stabilise larger neck diameters at small $\bar{r}_{core}$, and delay and counteract constriction slightly. Only for a growing $\bar{r}_{core} > 0.83$ is further stretching of the envelope facilitated by dilation of most necks, both in the simple membrane and with protein assemblies. With further increasing core radius, several necks dilate significantly ($\bar{r}_{core} = 0.87$ (see Supplementary Fig. 2)). However, long constant core-size simulations for different core radii ($\bar{r}_{core} > 0.83$) exhibit only one largely overdilated neck (see **Fig. 1c**). This indicates that multiple dilated necks are transient results of kinetics, and the lower free energy is achieved by a single overdilated configuration. If one neck overdilates all the other necks stay relatively constricted, as illustrated in **Fig. 1c** (and compared to frames from expanding core simulations, Supplementary Fig. 2).
The initial constriction in neck diameter (for $0.48 \leq \bar{r}_{core} \leq 0.83$) is accompanied by a reduction of over 50% in the inner-to-outer membrane (IM-OM) distance d in all simulations. The membrane distance starts to visibly recover and increase once overdilation occurs. These results suggest that, in addition to the neck diameter, the volume of Compartment II in a stomatocyte (**Fig. 1a**) is another variable to be adjusted, allowing for the possibility of neck constriction by stretching.

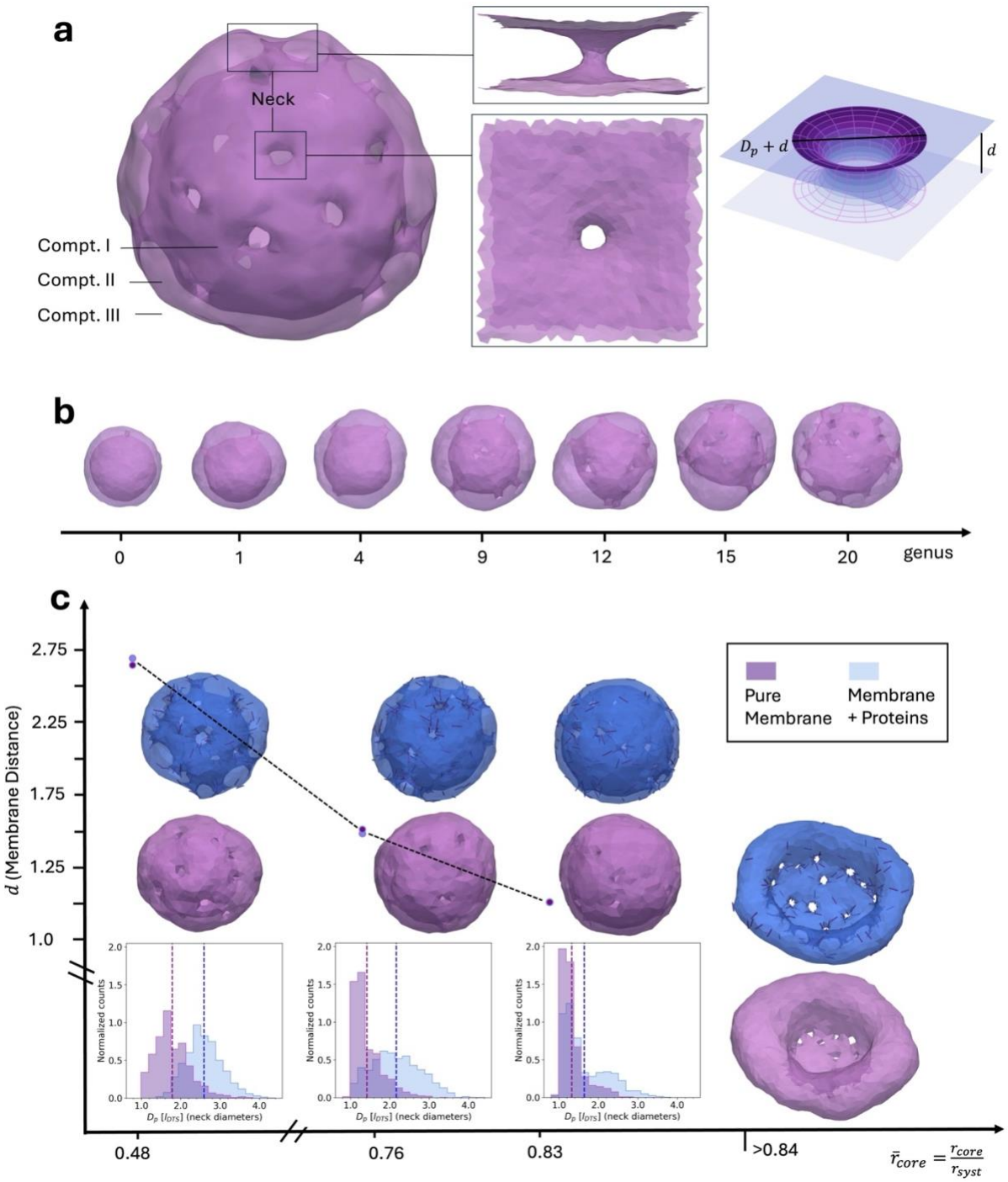

Fig. 1 **Simulations of high-genus stomatocytes**.
(a) A model of the high-genus (g=20) stomatocyte morphology (left), highlighting membrane necks and compartments created by the shape. Compt. I, the innermost part of the structure, corresponds to the nuclear lumen for NE, Compt. II, the volume between inner and outer membrane, representing the NE perinuclear volume. Compt. III lies beyond the outer membrane, e.g. the cytosol. The zoom-in to a membrane neck (middle) was used to examine neck behaviour close-up in PBC using DTS simulations. We also designed a simplified theoretical model (right) of a toroidal membrane neck. **(b)** Stomatocyte morphologies from genus 0 to genus 20 observed after equilibration for reduced volume $v = 0.3$ at bending rigidity of $\kappa = 20\ k_B T$. **(c)** A genus-20 stomatocyte (21 necks) at $\kappa = 10 k_B T$ was simulated with a continuously growing core bead to represent rising osmotic pressure in Compt. I, with and without curvature inducing proteins. The distributions were obtained from the last 50 frames (resp. 1050 necks) of subsequent equilibrium simulations at constant core radius. IM-OM distance (d) is given as the mean of the average d (over the membrane) of 50 frames; errors are not shown as they are smaller than the datapoint markers (standard error of the mean $SE(d) < 0.007 l_{DTS}$ for all d).

3. Two-state response of necks to stretching

To investigate the constriction/dilation effect further, we focused on the responses of necks in a subset of the system. The nuclear membrane is a large system ($5-20\ \mu m$ nucleus diameter [38]); therefore, the bending energy arising from its global spherical shape is negligible. A common model used in simulations for such systems are membranes (surfaces) with periodic boundary conditions (PBC) in the XY directions [39–42]. Here, we consider two flat surfaces connected by a single neck with PBC, representing a small segment of the NE (see **Fig. 1a**). Such model is particularly reasonable as the density of NPCs, while varying largely between species and tissues ($6-36\ /\mu m^2$), is relatively low in humans with $8-12\ /\mu m^2$ [43]. Hence the distance between NPCs can be estimated to around $150\ nm$ (see Supplementary Note 1). We present the simulation results, and afterwards consider a simple theoretical model to obtain additional intuition about these systems' behaviours.

We first performed constant frame tension simulations ((N,τ,T) ensemble, see also Supplementary Note 2), to account for the effect of the osmotic pressure in Compt. I (see also **Fig. 1a,b**). The results reveal a general behaviour: tension induced dilatation only when exceeding a threshold value, while below this threshold constriction occurred. The threshold for what constituted "sufficiently high" tension depended on the bending rigidity κ of the membrane and the starting diameter of the neck. Specifically, for our starting diameter of $D_p \approx 8l_{DTS}$ in a periodic box of $30 \times 30\ {l_{DTS}}^2$, we found dilation of necks for tensions starting at $1\ \frac{k_BT}{l_{DTS}^2}$ for $\kappa = 5k_BT$, $1.5\ \frac{k_BT}{l_{DTS}^2}$ for $\kappa = 10k_BT$ and $4\ \frac{k_BT}{l_{DTS}^2}$ for $\kappa = 20k_BT$. At lower tensions the neck underwent constriction, while at higher tensions it tended to dilate indefinitely (see Supplementary Fig. 3).

To further clarify, we performed constant projected area ensemble simulations (N, A_p, T) for a wide range of projected areas (for details see Methods). The resulting average bending energy as a function of A_p is shown in **Fig. 2a** for three different bending rigidities $5, 10$ and $20\ k_BT$. For all the depicted cases, we first observe a decrease in the mean bending energy with increasing projected area. Then, upon reaching a branching A_p, some replicas remain in the low-energy minimum, while others settle into a local minimum with higher energy. This marks the transition point or region, highlighted in the inset of **Fig. 2a**: the branching is preceded by a point of degeneracy, where replicas' equilibrium energies cover a range of values. Then, replicas equilibrate at either very low or higher energy states. Beyond a critical A_p, configurations in the lowest energy minimum disappear and the energy increases approximately linearly with projected area. The projected area at which the branching takes place is higher for larger bending rigidity. Conversely, a higher area compressibility (see Method section) pushes the branching point to smaller projected areas (**Fig. 2b** and Supplementary Fig. 4).

As shown in **Fig. 2a-d**, characteristic changes in neck size go along with the described energetic behaviour. While early increases in projected area are facilitated by neck constriction and decrease of IM-OM distance, greater increases of A_p lead to neck dilation and relaxation of the IM-OM distance. The decrease of bending energy at small projected areas can be attributed to neck constriction, but also to smoothing of the membrane far from the neck site (see snapshots **Fig. 2b**). At branching points, neck diameter dilation, corresponding to the higher-energy local minimum, as well as constriction, corresponding to the lower-energy minimum can occur. It should be noted that the coexistence of the two minima, despite one having significantly higher energy, could indicate an entropic preference for the dilated system compared to the highly constricted system. This is supported by the observation that the membrane becomes increasingly flat in the constricted system, suppressing many undulation modes (see **Fig. 2b**).

Overall, the neck diameter and IM-OM constriction followed by (over)dilation agrees with our observations in the stomatocyte simulations (see above). It becomes apparent that one key component to mechanistically explain the two-phase behaviour is the counteracting interplay of bending energy with the demand for larger projected area. We note that at effectively constant surface area A_0 ($K_A = 1000\ \mathrm{k_B T}$), the transition always takes place at $A_{p,branch} \lessapprox \frac{A_0}{2}$. This indicates that constriction occurs as long as the membrane surface area is large enough to span the specific projected area. Therefore, it can also explain why the transition point is shifted by bending rigidity and area compressibility. Higher bending rigidity increases available membrane surface area by smoothing undulation modes, while higher area compressibility resists surface extension. Hence, larger or smaller $A_{p,branch}$ can be facilitated, before the system reaches the physical constraints of how far it can stretch without neck dilation.

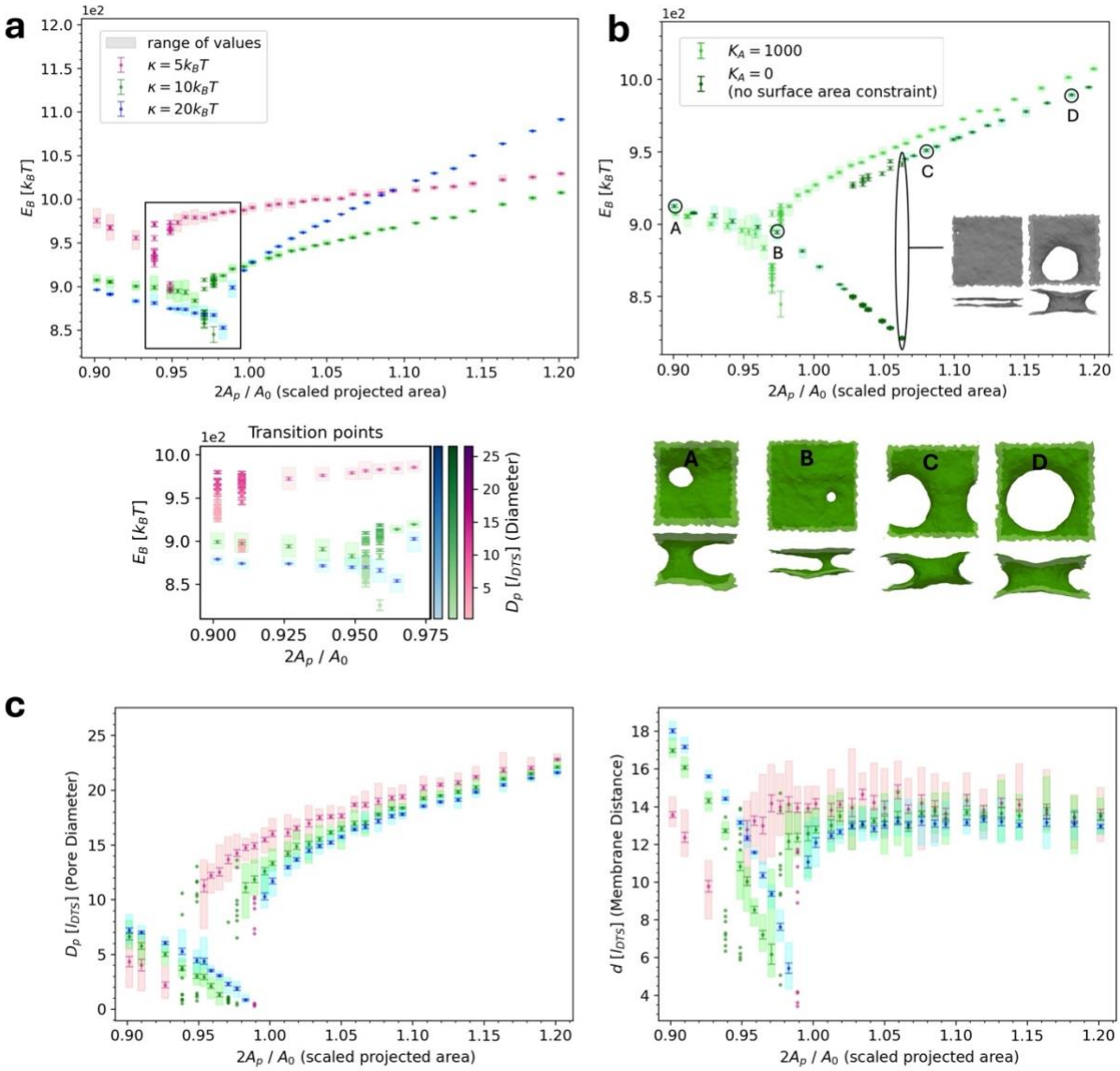

Fig. 2 **Constant box (constant projected area) simulations of double membranes connected by a neck in PBC.**
(a) Bending as a function of projected areas for different bending rigidities. Inset created from additional 30 replicas showing their individual behaviour at transition points, where the energies are related to observed diameters via a colour scale. Results were obtained from simulations with near-constant total surface area ($K_A = 1000\ k_BT$). For each parameters set and at each projected area 10 replicas were run (30 replica at transition points for inset). Each datapoint corresponds to their mean energy, errorbars indicate the standard error of the mean. At transition points in projected area some replicas show high, others low bending energy, indicating multiple local minima. Hence, all replicas are displayed instead of the mean; an error on each replica was obtained by block averaging over the last 10^6MC steps after equilibration of each simulation (20 blocks, length of 500 energy outputs; energy was saved every 100 MC steps).
(b) Influence of area compressibility K_A (see also Supplementary Fig. 4) and simulation snapshots of final morphologies. Results are shown for $\kappa = 10\ k_BT$ at near-constant surface area (see (a)) vs. no surface area constraint. Snapshots are shown for $K_A = 0\ \ k_BT$ but are representative for general behaviour, i.e. for all area compressibilities.
(c) Neck diameters (left) and membrane distance (right) after equilibration of one membrane neck in PBC at different projected areas. Results were obtained from simulations with near-constant surface area ($K_A = 1000\ \ k_BT$). Datapoints correspond to mean values of 10 replicas and errors were obtained as the standard error of the mean. Individual replicas at transition points are shown without errors. Note: while vertex distances always exceed $1\ l_{DTS}$, the analysis method may yield smaller values for extremely narrow necks. The procedure of obtaining neck sizes is detailed in the Methods section.

4. A simplified theoretical model predicts and characterizes constriction & dilation

To investigate the underlying effects further, we developed a theoretical model. Consider a region of the membrane around a neck in which beyond a certain cut-off radius ($\frac{D_p+d}{2}$) from the neck centre the membrane becomes flat (**Fig. 1c**). Thereby the neck is embedded in two square pieces of membrane with side length L, corresponding to IM and OM (inner and outer nuclear membrane in case of the NE). We assume that the neck is toroidal with diameters D_p and d, defining the smallest part of the channel and half of the IM-OM distance, respectively. For an evaluation of this assumption see Supplementary Note 5 (and Supplementary Fig. 12, 13). The bending energy of the system is described by the Helfrich Hamiltonian,

$$E_B = \oint \left[\frac{\kappa}{2}(2H)^2 - \kappa_G K\right] dA \quad (1),$$

with bending modulus κ, and gaussian modulus κ_G. The Gaussian term (second term) is constant if there is no topological change to the surface and therefore will be neglected. Then the bending energy of the toroidal neck is

$$E_B = f\left(\frac{D_p}{d}\right) = 4\pi\kappa \frac{D_p}{d} \frac{\left(1+\frac{d}{D_p}\right)^2}{\sqrt{1+\frac{2d}{D_p}}} tan^{-1}\left(\sqrt{\frac{2d}{D_p}+1}\right) \quad (2).$$

A lateral tension is represented by an energetic contribution $E_\tau = -\tau A_p$ with tension parameter τ and projected area A_p. Under the constraint of constant total surface area A_0, the rescaled energy ($\tilde{E} = E/4\pi\kappa$) will only depend on $\gamma := \frac{\tau}{\kappa} {D_p}^2$ and $\frac{d}{D_p}$. We minimised this energy numerically (for details see Supplementary Note 3). For zero frame tension ($\gamma = 0$) the bending energy has a minimum at $\frac{D_p}{d} \approx 0.6$ in agreement with other studies on toroidal pores [44,45] (Supplementary Note 3, Supplementary Fig. 5a). This points to a degeneracy of the neck size for tensionless membranes which qualitatively matches with our simulation results (Supplementary Fig. 5b). Non-vanishing frame tension, however, leads to degeneracy lifting. There, $\tilde{E}_{min}$ possesses a single local maximum, yielding an unstable critical point $\gamma_{\text{crit}} \approx 10.667$. This means that for systems with $\gamma < \gamma_{\text{crit}}$ ($\gamma > \gamma_{\text{crit}}$), at a given tension and bending rigidity, a membrane neck constricts (dilates) fully due to the tension (**Fig. 3a**). In other words, for a given neck diameter there exists a critical tension: below that value, the neck constricts, and above it, the neck dilates. This result is in good qualitative agreement with our simulations results. Moreover, $\gamma_{\text{crit}} = \tau_{crit} {D_p}^2/\kappa \approx 10.667$ provides a very simple but strong equation to assess the system behaviour. For example, the purified human NPC has a central channel diameter of about $43\,nm$ [31,46]. Assuming this as our neck diameter $D_p = 43nm$, and membrane bending rigidities in the range of $3 - 15 \times 10^{-20} J \approx 7 - 35 k_B T$ [47], our model predicts critical tension parameters of $\tau_{crit} \approx 1.7 - 8.7 \times 10^{-4} \frac{N}{m}$. NE tension has been

estimated to be about $\tau_{NE} \sim 1 \times 10^{-4} \frac{N}{m}$, an order of magnitude higher than typical plasma membrane [48–50]. Thus, the critical tension lies within the physiological range of the NE tension, making the described constriction and dilation phenomenon highly relevant for NPC responses to mechanical stimuli.

To evaluate the relationship between simplified theory and simulation results further, we solved the theoretical model for constant projected area. Details can be found in Supplementary Note 4. **Fig. 3b** shows the theoretical prediction of the neck diameters over a range of projected areas**,** similar to the simulation results in **Fig. 2c**. In contrast to the simulations, the theory predicts that the neck diameter is independent of membrane bending rigidity (the minimised energy is simply proportional to κ). However, we see very good agreement in the general behaviour of the predicted diameters with those obtained from simulations: while an increase in A_p first leads to constriction with increasingly negative slope, a transition point occurs, at which there is a jump to dilated states. From there on the diameter increases with projected area. Before the transition point is reached, an increase in projected area is facilitated by increasing constriction of neck diameters and IM-OM distance. This process is governed by bending energy in our model. It predicts a constant minimal bending energy value at all projected areas in the constrictive region, which depends on the bending rigidity (Supplementary Fig. 6c). The quantitative deviation of theory results from the simulations (see **Fig. 2a**) likely arises from the influence of thermally induced membrane undulations in the simulations.

The transition occurs at $A_{p,trans} = \frac{A_0}{2}$. Above this value, ($A_p > \frac{A_0}{2}$), the toroidal model has no longer any energetic upper constraint on D_p. This is due to an asymptotic convergence of the diameter ratio from above to $\lim_{D_p \to \infty} \frac{d(D_p)}{D_p} \approx 1.25$. However, the bending energy as a function of both diameters exclusively minimises at $\frac{D_p}{d} \approx 0.6$. Therefore, after the transition ($A_p > \frac{A_0}{2}$) the energy decreases with increase in D_p until the membrane size limit is reached. The diameters are hence not energetically constrained, but instead determined by the geometry of our setup, so $D_p + d \leq \sqrt{A_p}$. This limit leads to an approximately linear increase in D_p very similar to the one seen in simulations with large projected areas. The theoretical limit is not suitable to estimate the diameter values observed in simulations accurately (compare **Fig. 2a**). Likely, the difference is again caused by membrane undulations in the simulation, which lead to stricter constraints on D_p. Fitting the approximately linear energy increase after the transition point in simulations and comparing to the theoretical prediction shows that the ratio of the slopes for different bending rigidity agree well (for details see Supplementary Note 6), implying that the simulations in the dilation regime are predominantly steered by the same physics captured in the theory.

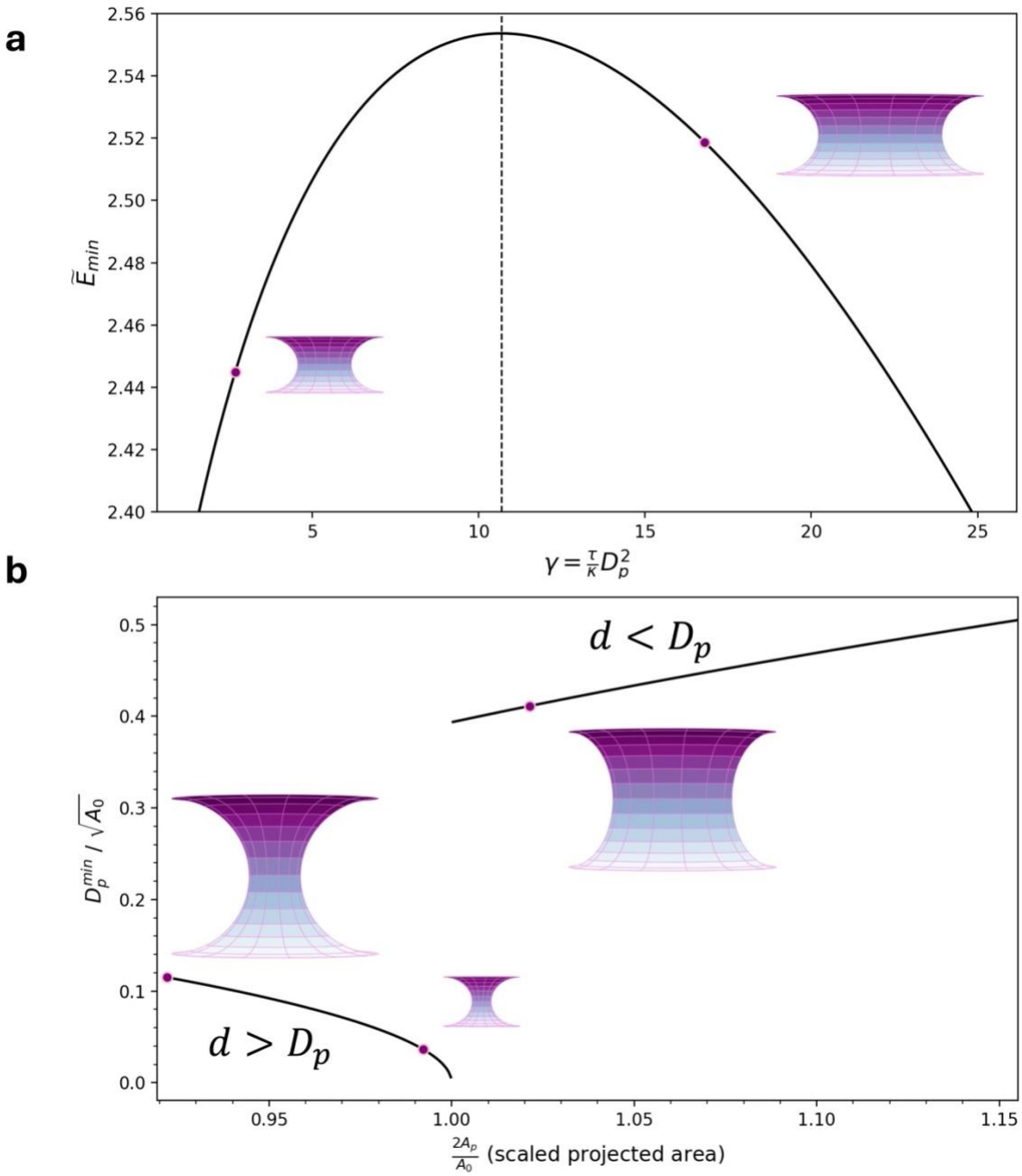

Fig. 3 **Theoretical predictions. (a)** Minimum rescaled energy ($\tilde{E} = \mathrm{E}/4\pi\kappa$) under constraint of constant surface area, as a function of dimensionless parameter γ. An energy barrier divides regions where constriction or dilation would be favoured at a specific tension and bending rigidity. A schematic view of the necks is shown. **(b)** Neck diameters D_p corresponding to minimal bending energies (see also Supplementary Fig. 6) under constraint of constant projected area and harmonic surface area potential with target surface area A_0 as functions of projected area. The neck diameters are scaled with the target area and are independent of bending rigidity. A regime of constriction, characterised by neck diameters smaller than the membrane distance d, is followed by dilation, where neck diameters are larger than the membrane distance. In the dilation regime, the neck diameters have finite sizes, as they are geometrically constrained by the system size, but they represent infinite dilation. This is because no local energy minimum exists once $A_p > \frac{A_0}{2}$, i.e. when neck diameters are larger than the membrane distance ($D_p > d$).

5. Multiple Neck Systems also show two state behaviour

Next, we examined how a system containing multiple necks in PBC responded to increasing projected area. For this purpose we chose systems of two, four and six necks per membrane in PBC. **Fig. 4a,b** (and Supplementary Fig. 7) shows the average bending energies after equilibration as a function of projected area A_p for different bending rigidities of $5, 10$ and $20\ k_BT$. (Here we have used area compressibility $K_A = 1000\ k_BT$). The multiple neck systems energetically behave very similar to the single neck system. For small increases in projected area, the bending energy decreases until a transition point is reached, after which it increases. The projected area at which the transition takes place increases with increasing bending rigidity. By inspecting the simulation snapshots, we find that this is also caused by constriction of all necks during small growth in projected area. For larger projected areas beyond the branching point, the system exhibits only one dilated neck. If additional dilated necks are present in the initial configurations (taken from simulations under tension), they transition to a more relaxed, constricted state during constant A_p simulation. This suggests that two or more dilated necks are transient features resulting from fast stretching dynamics, rather than representing the system's equilibrium configuration. The overall similarity to single-neck systems confirms that the underlying principles governing neck size in response to increasing projected area remain consistent across systems with different numbers of necks.

In systems with 6 necks, we did nevertheless see indications of multiple transition points occurring. These systems again showed constriction of all necks before the first transition point, and dilation of only one neck after it. However, this was followed by later dilation of more necks at larger projected areas (see **Fig. 4 a,b).** At the second possible transition point in the data for $\kappa = 10k_BT$, the snapshots from the simulations highlight that the replicas with fewer dilated and more constricting necks have lower bending energy. This helps to explain the observation that only one dilated neck was found in equilibrated systems of genus two and four, and earlier in stomatocyte vesicles (see also **Fig. 1c**). Taken together, it seems to be more energetically efficient to have one neck dilated by a larger amount than two (or multiple) necks dilated by a smaller amount each. The energetic cost of dilation of more than one neck at larger projected areas seen in the 6-neck system may be compensated by an entropic gain. While multiple-neck systems behave similarly to the single-neck system overall, their response is more complex. Significant degeneracy may exist within the dilation regimes; further exploration of these feature is beyond the scope of this work.

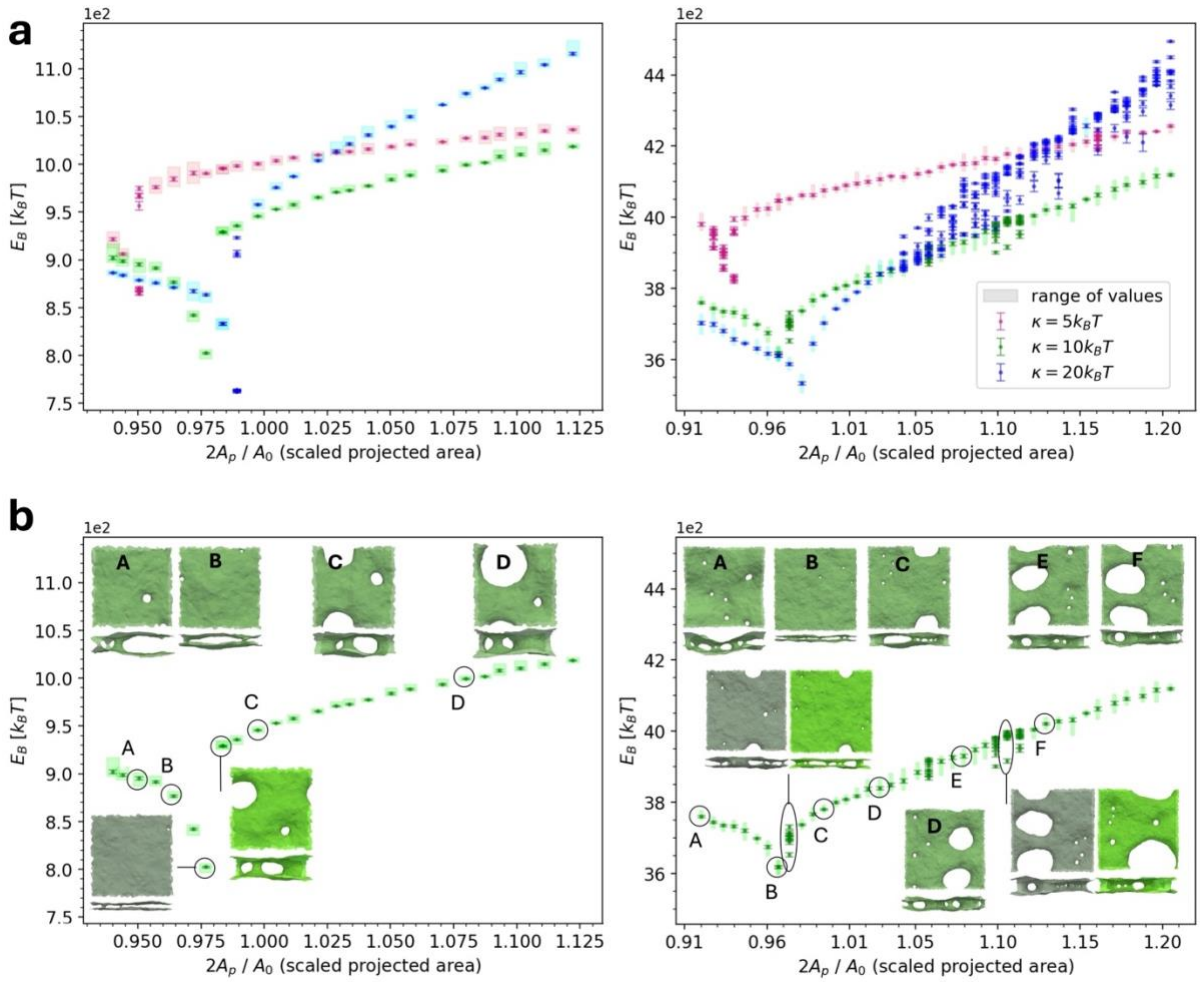

Fig. 4 **Systems with multiple necks in PBC. (a)** Bending energy after equilibration of two (left) and six (right) membrane necks in PBC at different projected areas. Results were obtained from simulation with near-constant surface area $A_0 = 2541\ l_{DTS}^2$ ($10524\ l_{DTS}^2$) ($K_A = 1000\ k_BT$). While two necks (and four necks, see SI) show one transition point like a single neck, at six necks multiple such transitions exist, possibly overlayed. The occurrence depends on the bending rigidity. At each projected area 10 replicas of the simulations were run. Each datapoint corresponds to their mean energy and errorbars indicate the standard error of the mean. At (possible) transition points in projected area, all replicas are displayed instead of the mean; an error on each replica was obtained by block averaging: for two (six) necks over the last 10^6MC steps (8×10^5 MC steps) of each simulation after equilibration (20 blocks (16 blocks), length of 500 energy outputs; energy was saved every 100 MC steps). **(b)** Visualisation of the necks' behaviour for two (left) and six (right) necks in PBC at bending rigidity of $\kappa = 10\ k_BT$. This illustrates a second transition point or region in the six-neck-system, facilitated by successive dilation of more than one neck.

5. Protein Addition to the Neck Retains the Key behaviours

Finally, we tested systems containing a neck decorated by a protein complex (for details, see Methods). We employed a minimal model for the protein complex, using elongated inclusions with a preferred negative curvature that assemble into the neck, effectively forming a protein complex (see Fig. 5). By varying attractive protein-protein interactions, we explored different stability of the complex structure. This model implicitly mimics the complex's interaction with the membrane. The system was initially equilibrated in a tensionless state of the membrane, to allow for proteins to assemble in the membrane neck. Then it was subjected to a range of frame tensions under the constraint of near-constant total surface area ($K_A = 1000 k_B T$).

We first examined how protein abundance, i.e. size of the complex, induced curvature and interaction strength influence the response of membrane neck size to increasing tension (for details see Supplementary Fig. 8). A larger complex with strong protein interactions suppresses neck constriction at lower tensions and causes a controlled slight neck dilation with prevention of overdilation at increased tension. Compared to smaller protein complexes with less interaction, it surprisingly causes earlier occurrence of overdilation for $\tau > 6\ \frac{k_B T}{l_{DTS}^2}$. Increasing the induced curvature (from $-0.8\ l_{DTS}^{-1}$ to $-1.0\ l_{DTS}^{-1}$) or decreasing the interactions between proteins prolongs neck stability (overdilation at higher tension). The lowered interaction strength furthermore allows for a notable constriction response to increasing tension. Decreasing the size of the protein complex as well leads to an even stronger constriction response to tension, accompanied by neck stability for at least $\tau \leq 8\ \frac{k_B T}{l_{DTS}^2}$. Taken together, this shows that the proteins retain the key membrane responses to tension but counteract and control them increasingly the larger and/or stiffer the protein complex is.
We studied the response in more detail by performing constant projected area ensemble simulations, and examining the behaviour of energy (Supplementary Fig. 9) and neck diameters (**Fig. 5**) as a function of projected area for the large protein complex (5% coverage), as well as for a smaller protein complex (3% coverage) with varying interactions. This underlines the observations under tension, by showing that the large, cohesive complex can indeed suppress constriction, especially through strong interaction between the proteins. Compared to a simple membrane, the complex first stabilises a moderately small neck, while the IM-OM distance decreases (see **Fig. 5**), until dilation sets in at larger projected areas. This dilation can occur more continuously compared to the abrupt behaviour seen in a pure membrane. A less cohesive or smaller protein complex instead retains all key behaviours of the pure membrane, displaying constrictions for smaller projected areas followed by dilation after $A_{p,branch} \lessapprox \frac{A_0}{2}$. The constriction and dilation are more pronounced and the transition more abrupt the weaker the interactions between proteins are. Neither the protein abundance nor the interaction strength largely influence the location of the transition point ($\Delta\ (2A_{p,branch}\ /A_0) \lessapprox 0.008$ for all comparisons).

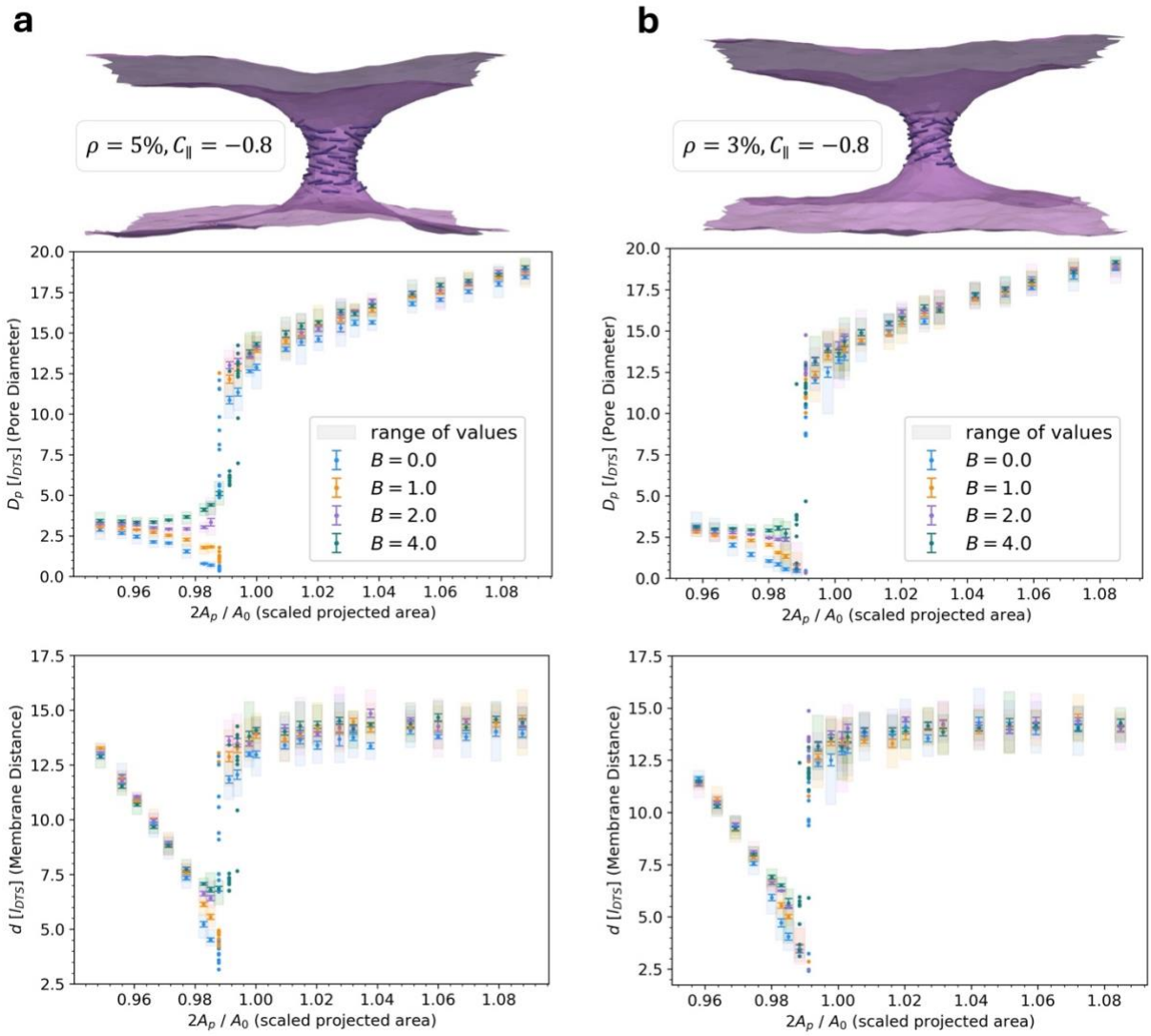

Fig. 5 **Constant box (constant projected area) simulations of double membranes connected by a neck with protein assembly in PBC**.

Neck diameters (top) and membrane distances (bottom) of simulations over a range of constant projected areas, for different protein complex sizes of **(a)** a coverage of $\rho = 5\%$ of membrane vertices with an inclusion, and **(b)** a coverage of $\rho = 3\%$ of membrane vertices with an inclusion, i.e. a protein.

The protein interaction strengths were varied ($A = 1k_BT, B$ in k_BT as specified in legend) at constant curvature preference ($C_{\parallel}$in $[l_{DTS}^{-1}]$). Results were obtained from simulations with near-constant surface area ($K_A = 1000\ k_BT$). Datapoints correspond to mean values of 10 replicas and errors were obtained as the standard error of the mean. Individual replicas at transition points are shown without errors. Note: while vertex distances always exceed $1\ l_{DTS}$, the analysis method may yield smaller values for extremely narrow necks. The procedure of obtaining neck sizes is detailed in the Methods section. The simulation snapshots visualize the protein assembly, which was the basis for these simulations and was formed beforehand by equilibrating the membrane decorated by inclusions in a tensionless regime. The proteins are depicted as tubes to indicate their orientation.

DISCUSSION & CONCLUSION

Stomatocyte shapes are highly relevant in both biological and synthetic membranes. They can divide space into three distinct compartments. Two of these compartments are connected via narrow necks, which can serve as intriguing sites for the assembly of specific biomolecular complexes to regulate material transport between them. Understanding how the size of these necks responds to external stimuli is therefore important to elucidate cellular processes (e.g. nuclear mechanosensing). In this work, we used theoretical analysis and mesoscale computer simulations to investigate this behaviour. Our findings indicate that at low membrane tension or small pressure differences between the innermost and outer compartments, the necks constrict. Conversely, at higher tension, they dilate and open. Parameters such as bending rigidity and area compressibility govern the transition between these two phases. The two phase behaviour arises solely from the mechanical properties of the membrane in the stomatocyte configuration, particularly in surfaces with high topological genus. It can be modified by the presence of protein assemblies, stabilising against constriction and dilation to some degree depending on their properties (induced curvature, interaction strength, size of the assembly), but the key two-phase tension response remains.

This two-state response may explain several of the observed behaviours in the experimental setting, especially the dilation of intact NPCs but also the constriction of defect NPCs under tension. Since our model predicts threshold tensions in the physiological range, constriction too should play a role in the nuclear pores' adaptation to mechanical stress. It could then e.g. explain the unexpected observations in cases of defect NPCs [30], challenging the assumption that dilation is the sole response to internal (osmotic) pressure or lateral tension. While the influence of the protein complex was not explicitly modelled, our results support the notion that an intact NPC safeguards nuclear pores against overdilation [30]. We also propose that the nuclear membrane itself transmits the forces to the NPC, as, according to our findings, the behaviour of the simple membrane alone supports the previously reported NPC adjustments to changes in tension. Therefore, other potential sources of force transmission, like the LINC complex [51], might not be needed. However, the NE is far more complex than our minimal model, which is designed to capture only the generic behaviour. Firstly, the NPC is an assembly of proteins that interact in a complicated manner which is not fully captured in our model. Secondly, the NE is covered by several groups of proteins, which additionally interact with nuclear lamina and chromatin [52–54], adding complexity to the membrane mechanics. Hence, our results here are generic and we expect them to represent only the qualitative and fundamental behaviours of the NE and NPC system. Indeed, for a more detailed understanding, methods such as multiscale simulations [55,56] that incorporate the details of the molecular systems while reaching the relevant time and length scales are needed. This might also include a more detailed comparison to experimental results and combining simulation and experimental studies to complement each other [57]. Yet, the generality of our model is also a key strength. While it does not capture fine-grained details, it demonstrates

robustness against variations in the chosen force field and potential unaccounted effects, suggesting the universality of the observed behaviour.

Neck dilation in stomatocytes is fundamentally different from that of spherical closed vesicles. It is governed by distinct physical mechanisms and results in different features. In spherical closed vesicles, strong pressure differences cause the membrane to stretch. Once a critical tension is exceeded, a pore forms, which can eventually develop into a hole if the pressure release is too slow. The stretched membrane then relaxes into a tensionless state, allowing the hole to expand further and ultimately compromise the vesicle's structural integrity. In contrast, neck dilation in stomatocytes occurs without pore or hole formation, and the membrane remains intact. Moreover, the tension required for neck dilation in stomatocytes is significantly lower ($\approx 3-4\times 10^{-4}\,\frac{N}{m}$ for $\kappa \approx 15k_BT$, see above) than that needed for hole formation in vesicles ($\approx 1-10\ \times 10^{-3}\,\frac{N}{m}$, membrane rupture tension [58,59]). This indicates that stomatocytes offer a finely tuned mechanism for compartmentalisation, providing a level of precision different from the commonly used amphiphilic assemblies like bilayers. This distinctive feature highlights the potential of high-genus membranes as functional units in synthetic biology and membrane engineering.

Since our results are based on a very generalised system, the findings could extend to other membrane systems with necks under tension, like the endoplasmic reticulum (ER). Interestingly, simulations with neck (over)dilation in PBC gave stretched configurations that had formed three-way junctions characteristic of the ER structure (see Supplementary Fig. 10). ER three-way junctions are argued to arise from a substantial membrane tension [60,61], making it is unsurprising that our observations may be applicable to such systems, due to their generation during neck dilation under lateral tension. In turn, computational studies on ER membranes during transformation of junctional knots to regular junctions have shown an interesting similarity to the neck behaviour in stomatocytes. There, small membrane necks (also referred to as pores) constrict in the centre of an ER junctional knot under tension [62]. This points to the relevance of the mechanism of membrane neck dilation and constriction in other cellular structures and processes apart from mechanosensing of the nuclear envelope.

Moreover, bridging back from ER to NE, our results may offer further understanding to postmitotic NPC assembly, which was previously reported as a sequence of membrane neck constriction and dilation events. Initially, fenestrated ER sheets' holes (equal to largely overdilated membrane necks) shrink. Then NPC precursors accumulate in these small necks and dilate them during complex assembly and maturation [63]. Based on our results, it stands to reason that membrane lateral tension could play a significant role in this process. Initial ER neck constriction may be facilitated by membrane tension alongside ER proteins actively driving the reshaping. Our findings on protein assemblies in necks furthermore support the idea that the precursor NPC accumulation stabilises the ER–NE hole shrinkage [63], allowing for prepores (preNPCs) to dilate to final size as they mature. As one can assume that prepores

correspond to small protein assemblies with weaker interactions, these would counteract tension-driven constriction only slightly. Maturing NPCs then become larger and more cohesive. That could counteract constriction and possibly drive the neck diameter beyond the threshold, after which membrane tension would cause dilation. This is ultimately stabilised by the fully assembled NPCs when the final size is reached.

In conclusion, our study reveals a previously overlooked, general material property of high genus stomatocyte membranes. We demonstrate that internal osmotic pressure (or lateral tension) can lead to membrane neck constriction at low and dilation at high tensions. These results have implications not only for the nuclear envelope but also for other biological systems with (many) membrane necks. This includes the high-genus membranes of other cell organelles, like the ER, mitochondria and Golgi apparatus.

METHODS

The mesoscopic simulations were performed using Dynamically Triangulated Surface simulations that have been shown to be very effective for simulating cell membranes at large scales [64,65]. There are a few different models and software packages available for performing mesoscale simulations [66–70]. Here, we have used FreeDTS [5], which has shown to reproduce correct thermodynamical behaviours of lipid bilayers such as the undulation spectrum [39,71]. FreeDTS represents the membrane as a surface of N_v vertices, N_e edges and N_T triangles. The software uses the shape operator formulation to calculate membrane curvature at each vertex [39]. A vertex is assigned with a unit normal $\widehat{\mathrm{N}}_v$, surface area A_v, principal curvatures (c_{1v}, c_{2v}) and principal directions $(\mathrm{X}_1(v), \mathrm{X}_2(v))$ via a set of discretised geometrical operations. The bending energy of the surface (E_B) is given by a discretised form of the Helfrich Hamiltonian in terms of the mean $H = \frac{c_1+c_2}{2}$, and Gaussian curvature, $K = c_1 c_2$ as:

$$E_B = \frac{\kappa}{2}\sum_{1}^{N_v}(2H_v - \bar{C}_0)^2 A_v + \kappa_G \sum_{1}^{N_v} K_v A_v \quad (3)$$

with the bending modulus κ, Gaussian modulus κ_G, and spontaneous curvature $\bar{C}_0$. The latter represents a possible asymmetry between the two monolayers ($\bar{C}_0 = 0$ for a symmetric membrane). The simulations are evolved using a metropolis algorithm. A Monte Carlo (MC) step corresponds to N_v attempts to move a vertex and N_e attempts to flip links.
Constant tension simulations in PBC employ a position rescaling algorithm to adjust the box size [39]. For every Xth Monte Carlo (MC) step, an additional box change attempt is made. This algorithm couples the system energy to

$$E_\tau = -\tau A_p \quad (4),$$

where A_p is the projected area.
An area constraint algorithm can be added to control the surface area of a membrane, since

due to flexibility of the edge length, the area of each triangle can vary and the membrane surface is stretchable. In that case, the energy is coupled to an additional term of

$$E_A = N_T \frac{K_A}{2}\left(\frac{A}{A_0} - 1\right)^2 \quad (5),$$

with the compressibility modulus K_A and the targeted surface area A_0. For constant volume simulations, the system energy was coupled to a potential of:

$$E_V = \frac{K_V}{2}\left(\frac{V}{V_0} - \alpha\right)^2 \quad (6).$$

Generating configurations for high-genus vesicles and flat double membranes with PBC

Stomatocyte structures for this setup were obtained by relaxing and equilibrating a cuboid membrane configuration with n necks for genus n (for details see Supplementary Fig. 11). An expanding hard core potential was then placed at the centre of the shape, with an initial exclusion radius of $5l_{DTS}$. This radius was chosen to fit inside the innermost compartment of the stomatocyte. Expanding core simulations were performed over 5×10^6 MC steps, with three replica each. The hard core potential was set to continually expand at $0.05 \times 10^{-3} \frac{l_{DTS}}{MC\ step}$. Since no surface vertex is allowed to lie inside the spherical core, the membrane must expand the centre compartment accordingly. No additional volume control was applied. The surface area was effectively fixed with area compressibility $K_A = 1000\ k_BT$ (see formula (5)). From these simulations, frames were taken at different sizes of core radius and equilibrated at that fixed radius over $3 - 5 \times 10^6$ MC steps. Equilibrated morphologies were analysed for neck diameters and IM-OM distance. Details on their calculation can be found below.

Configurations for high-genus surfaces in PBC were obtained by relaxing and equilibrating a cuboid membrane configuration with open sides with one to six necks (genus 1-6) in periodic boundary conditions (for details see Supplementary Fig. 11). The simulations incorporate membrane fluctuations and allow for variable neck shapes dictated purely by free energy optimisation. To include the effect of mechanical stresses present during exponential cell growth or differentiation, which are assumed to act as tension on the NE membrane [29,30,51], we subjected our membrane to lateral tension with parameter τ (in the x-y-plane) and, taking into account Helfrich bending energy, determined its minimal free energy state.
For simulations over a range of projected areas, individual frames were chosen from a simulation trajectory under tension. These frames were then equilibrated at constant projected area $(A_p)_i$ for the i-th frame, over 2×10^6 MC steps. This was performed with a potential promoting constant surface area for area compressibilities of $K_A = 0,\ 10,\ 100,\ 1000\ k_BT$ (see formula (5)). Equilibrated morphologies were analysed for bending energy, neck diameters, IM-OM distance and surface area at all projected areas $(A_p)_i$.

Analysis

For high-genus vesicles, neck diameter distributions and IM-OM distances were obtained from the last 50 frames of equilibrated simulations. At each frame, corresponding to one membrane mesh configuration, we first constructed the convex hull of this mesh. The mesh was then sectioned into IM and OM by distance of vertices to the convex hull, as the OM naturally lies very close to the hull, while the IM does not (see **Fig. 6a**, left). The threshold distance below (above) which a vertex was assigned to the OM (IM) was determined for each mesh individually, as it is influenced by the shape of each mesh and the IM-OM distance. The average IM-OM distance for each membrane configuration was subsequently determined by calculating the difference in the average distance of IM and OM to the vesicle centre (**Fig. 6a**, middle). Neck diameters D_p were calculated from the IM (or OM) through determining the circumference C of the necks, which were cut open due to separation of IM and OM mesh (see **Fig. 6a**, right).

For membranes in PBC, the average IM-OM distance was obtained by determining the average z-position of the two membrane sheets in the box and then calculating their distance (**Fig. 6b**, left). The neck diameter D_p was determined by projecting the mesh onto the x-y-plane and converting it to a binary image (**Fig. 6b,** middle & right). From the binary image, the area of the hole region A_H was determined by converting pixels to the simulation lengthscale using the boxsize known from the simulation. Then $D_p = \sqrt{4A_H/\pi}$. For extremely small neck sizes, this can underestimate neck size.

Every simulation in PBC was run with 10 replicas. Each datapoint for IM-OM distances, neck diameters and bending energies hence corresponds to the mean of the values recovered for these 10 replicas and errorbars indicate the standard error of the mean. Around branching points in projected area some replicas show high, others lower bending energy, indicating multiple local minima or degeneracy. When replica results are displayed individually instead of mean values, an error on the energy of each replica was obtained by block averaging over the last 10^6 MC steps after equilibration of each simulation (20 blocks, length of 500 energy outputs; energy was saved every 100 MC steps). Only in case of genus-6, due to the larger system size, 8×10^5 MC steps after equilibration were used for the analysis (16 blocks, length of 500 energy outputs; energy was saved every 100 MC steps).

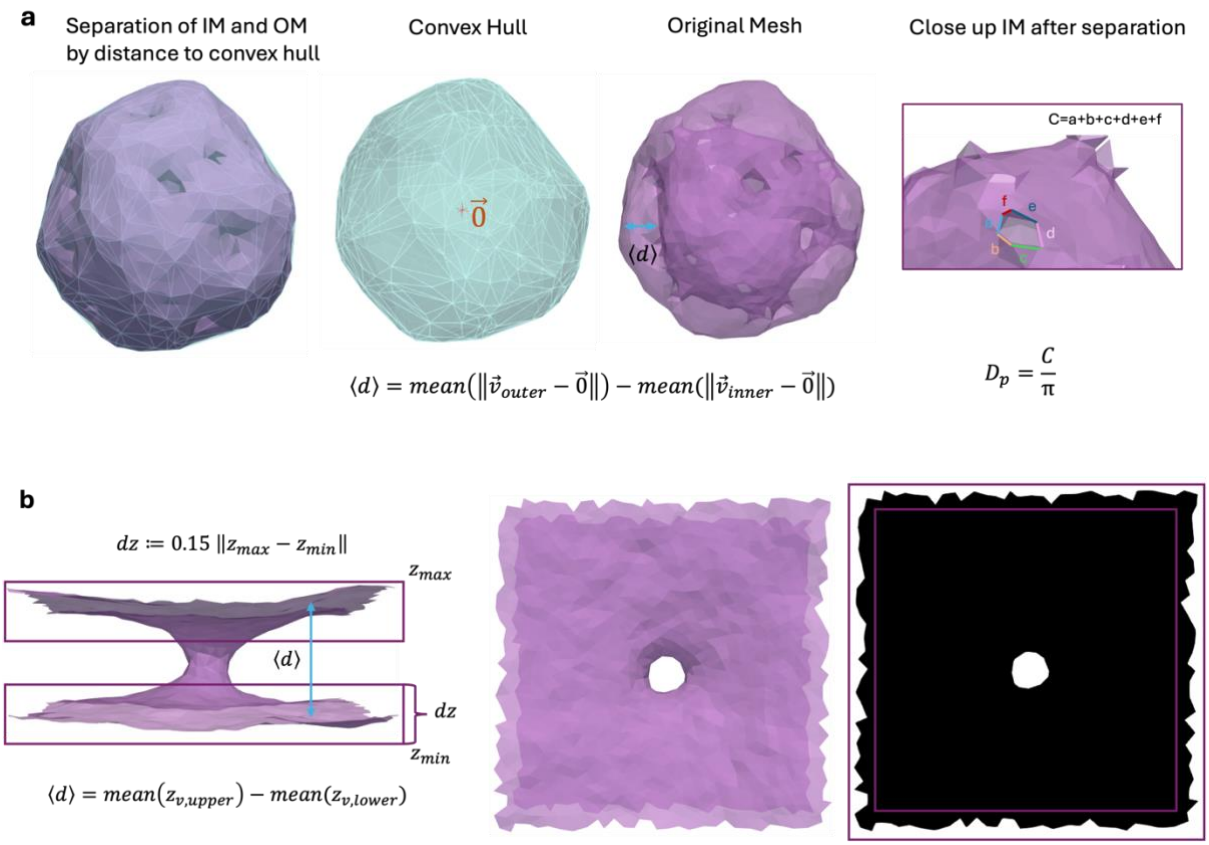

Fig. 6 **Process of determining IM-OM distance and membrane neck diameters**.
(a) For high-genus vesicle membranes, the convex hull was used as a criterion to divide the mesh into IM and OM. Vertices closer to the hull than a threshold value were assigned to the OM. Based on this separation into two meshes, membrane distance and neck diameters were determined.
(b) For membranes in PBC, IM and OM were determined by the z-coordinate of vertices on the mesh as shown. Neck diameters were calculated based on a 2d-projection of the mesh.

Proteins

Proteins in FreeDTS are modelled as inclusions with an in-plane orientation, so that there is at most one inclusion per membrane vertex [5]. To emulate protein complexes that assemble in membrane necks, we chose proteins with asymmetric interactions with the membrane (inclusion type 2 in FreeDTS),

$$e_{mem-pro} = \left\{\frac{k_1}{2}(C_\parallel - C_{\parallel 0})^2 + \frac{k_2}{2}(C_\perp - C_{\perp 0})^2\right\} A_v \quad (7),$$

where $C_\parallel$ ($C_\perp$) denote membrane curvature parallel (perpendicular) to the inclusion orientation and k_1, k_2 are directional bending rigidities that the protein enforces on the membrane. Protein–protein interactions are modelled as a function of the angle between two inclusions i, j along the geodesic $\Theta = \Theta_j - \Theta_i$,

$$e_{pro-pro} = -A - B\cos(2\Theta) \quad (8).$$

For more details see [5].

Stomatocytes were decorated by 10% of inclusions with $C_{\parallel 0} = \frac{1}{l_{DTS}}$, $C_{\perp 0} = \frac{-1}{l_{DTS}}$, $k_1 = 10 k_B T$,

$k_2 = 5k_BT$ and zero protein-protein interactions as this was enough for the proteins to cluster around the necks. Single membrane necks in PBC were decorated by 2.5-5% of inclusions with $C_{\|0}$ in the range of $-[0.8\,,1.0]\ l_{DTS}^{-1}$, $k_1 = 10k_BT$. In these systems, attractive inclusion-inclusion interactions were used, $A = 1$ and $B = (0,1,2,4)$, to explore larger parameter sets.

Acknowledgements

We thank Mary Wood for comments and feedback on this manuscript. This research was supported by Novo Nordisk Foundation (grant No. NNF18SA0035142 and NNF22OC0079182) and Independent Research Fund Denmark (grant No. 10.46540/2064-00032B). WP received support from the Skłodowska-Curie Fellowship (grant no. 101104867).

Author Contributions

WP conceived the original idea. BG performed simulations, obtained the results and developed the theory. BG and WP wrote the manuscript. All authors discussed the results and commented on the manuscript at all stages.

Competing Interests

The authors declare no competing interests.

BIBLIOGRAPHY

1. Gallagher, P. G. Chapter 45 - Red Blood Cell Membrane Disorders. in *Hematology (Seventh Edition)* (eds. Hoffman, R. et al.) 626–647 (Elsevier, 2018). doi:10.1016/B978-0-323-35762-3.00045-7.
2. Lipowsky, R. The conformation of membranes. *Nature* **349**, 475–481 (1991).
3. Seifert, U., Berndl, K. & Lipowsky, R. Shape transformations of vesicles: Phase diagram for spontaneous- curvature and bilayer-coupling models. *Phys. Rev. A* **44**, 1182–1202 (1991).
4. De Franceschi, N. *et al.* Synthetic Membrane Shaper for Controlled Liposome Deformation. *ACS Nano* **17**, 966–978 (2023).
5. Pezeshkian, W. & Ipsen, J. H. Mesoscale simulation of biomembranes with FreeDTS. *Nat. Commun.* **15**, 548 (2024).
6. Jülicher, F., Seifert, U. & Lipowsky, R. Conformal degeneracy and conformal diffusion of vesicles. *Phys. Rev. Lett.* **71**, 452–455 (1993).
7. Noguchi, H. Construction of Nuclear Envelope Shape by a High-Genus Vesicle with Pore-Size Constraint. *Biophys. J.* **111**, 824–831 (2016).
8. Noguchi, H. Shape transitions of high-genus fluid vesicles. *Europhys. Lett.* **112**, 58004 (2015).
9. Otsuka, S. *et al.* Postmitotic nuclear pore assembly proceeds by radial dilation of small membrane openings. *Nat. Struct. Mol. Biol.* **25**, 21–28 (2018).
10. Parzych, K. R. & Klionsky, D. J. An Overview of Autophagy: Morphology, Mechanism, and Regulation. *Antioxid. Redox Signal.* **20**, 460–473 (2014).

11. De Magistris, P. & Antonin, W. The Dynamic Nature of the Nuclear Envelope. *Curr. Biol.* **28**, R487–R497 (2018).

12. Bieber, A. *et al.* In situ structural analysis reveals membrane shape transitions during autophagosome formation. *Proc. Natl. Acad. Sci. U. S. A.* **119**, e2209823119 (2022).

13. Sakai, Y., Takahashi, S., Koyama-Honda, I., Saito, C. & Mizushima, N. Experimental determination and mathematical modeling of standard shapes of forming autophagosomes. *Nat. Commun.* **15**, 91 (2024).

14. Sakai, Y., Koyama-Honda, I., Tachikawa, M., Knorr, R. L. & Mizushima, N. Modeling Membrane Morphological Change during Autophagosome Formation. *iScience* **23**, 101466 (2020).

15. Hetzer, M. W. The Nuclear Envelope. *Cold Spring Harb. Perspect. Biol.* **2**, a000539 (2010).

16. Webster, M., Witkin, K. L. & Cohen-Fix, O. Sizing up the nucleus: nuclear shape, size and nuclear-envelope assembly. *J. Cell Sci.* **122**, 1477–1486 (2009).

17. Strambio-De-Castillia, C., Niepel, M. & Rout, M. P. The nuclear pore complex: bridging nuclear transport and gene regulation. *Nat. Rev. Mol. Cell Biol.* **11**, 490–501 (2010).

18. Fabre, E. & Hurt, E. YEAST GENETICS TO DISSECT THE NUCLEAR PORE COMPLEX AND NUCLEOCYTOPLASMIC TRAFFICKING. *Annu. Rev. Genet.* **31**, 277–313 (1997).

19. Grossman, E., Medalia, O. & Zwerger, M. Functional Architecture of the Nuclear Pore Complex. *Annu. Rev. Biophys.* **41**, 557–584 (2012).

20. Hoelz, A., Debler, E. W. & Blobel, G. The Structure of the Nuclear Pore Complex. *Annu. Rev. Biochem.* **80**, 613–643 (2011).

21. Patel, M. K., Chakrabarti, B. & Panwar, A. S. Emergence of selectivity and specificity in a coarse-grained model of the nuclear pore complex with sequence-agnostic FG-Nups. *Phys. Chem. Chem. Phys.* **25**, 32824–32836 (2023).
22. Efremov, A. K., Hovan, L. & Yan, J. Nucleus size and its effect on nucleosome stability in living cells. *Biophys. J.* **121**, 4189–4204 (2022).
23. Stephens, A. D., Banigan, E. J., Adam, S. A., Goldman, R. D. & Marko, J. F. Chromatin and lamin A determine two different mechanical response regimes of the cell nucleus. *Mol. Biol. Cell* **28**, 1984–1996 (2017).
24. Mazumder, A., Roopa, T., Basu, A., Mahadevan, L. & Shivashankar, G. V. Dynamics of Chromatin Decondensation Reveals the Structural Integrity of a Mechanically Prestressed Nucleus. *Biophys. J.* **95**, 3028–3035 (2008).
25. Finan, J. D., Chalut, K. J., Wax, A. & Guilak, F. Nonlinear Osmotic Properties of the Cell Nucleus. *Ann. Biomed. Eng.* **37**, 477–491 (2009).
26. Dahl, K. N., Kahn, S. M., Wilson, K. L. & Discher, D. E. The nuclear envelope lamina network has elasticity and a compressibility limit suggestive of a molecular shock absorber. *J. Cell Sci.* **117**, 4779–4786 (2004).
27. Deviri, D. & Safran, S. A. Balance of osmotic pressures determines the volume of the cell nucleus. 2021.10.01.462771 Preprint at https://doi.org/10.1101/2021.10.01.462771 (2021).
28. Lemière, J., Real-Calderon, P., Holt, L. J., Fai, T. G. & Chang, F. Control of nuclear size by osmotic forces in Schizosaccharomyces pombe. *eLife* **11**, e76075 (2022).
29. Zimmerli, C. E. *et al.* Nuclear pores dilate and constrict in cellulo. *Science* **374**, eabd9776 (2021).

30. Taniguchi, R. *et al.* Nuclear pores safeguard the integrity of the nuclear envelope. 2024.02.05.578890 Preprint at https://doi.org/10.1101/2024.02.05.578890 (2024).

31. Schuller, A. P. *et al.* The cellular environment shapes the nuclear pore complex architecture. *Nature* **598**, 667–671 (2021).

32. Mosalaganti, S. *et al.* AI-based structure prediction empowers integrative structural analysis of human nuclear pores. *Science* **376**, eabm9506 (2022).

33. Hoffmann, P. C. *et al.* Nuclear pore permeability and fluid flow are modulated by its dilation state. *Mol. Cell* **85**, 537-554.e11 (2025).

34. Bui, K. H. *et al.* Integrated Structural Analysis of the Human Nuclear Pore Complex Scaffold. *Cell* **155**, 1233–1243 (2013).

35. Yu, M. *et al.* Visualizing the disordered nuclear transport machinery in situ. *Nature* **617**, 162–169 (2023).

36. Roffay, C. *et al.* Passive coupling of membrane tension and cell volume during active response of cells to osmosis. *Proc. Natl. Acad. Sci.* **118**, e2103228118 (2021).

37. Alam Shibly, S. U., Ghatak, C., Sayem Karal, M. A., Moniruzzaman, Md. & Yamazaki, M. Experimental Estimation of Membrane Tension Induced by Osmotic Pressure. *Biophys. J.* **111**, 2190–2201 (2016).

38. Lammerding, J. Mechanics of the Nucleus. *Compr. Physiol.* **1**, 783–807 (2011).

39. Pezeshkian, W. & Ipsen, J. H. Fluctuations and conformational stability of a membrane patch with curvature inducing inclusions. *Soft Matter* **15**, 9974–9981 (2019).

40. Neder, J., West, B., Nielaba, P. & Schmid, F. Coarse-grained simulations of membranes under tension. *J. Chem. Phys.* **132**, 115101 (2010).

41. Shiba, H., Noguchi, H. & Fournier, J.-B. Monte Carlo study of the frame, fluctuation and internal tensions of fluctuating membranes with fixed area. *Soft Matter* **12**, 2373–2380 (2016).

42. Durand, M. Frame tension governs the thermal fluctuations of a fluid membrane: new evidence. *Soft Matter* **18**, 3891–3901 (2022).

43. Maul, G. & Deaven, L. Quantitative determination of nuclear pore complexes in cycling cells with differing DNA content. *J. Cell Biol.* **73**, 748–760 (1977).

44. Chizmadzhev, Y. A., Cohen, F. S., Shcherbakov, A. & Zimmerberg, J. Membrane mechanics can account for fusion pore dilation in stages. *Biophys. J.* **69**, 2489–2500 (1995).

45. Jackson, M. B. Minimum Membrane Bending Energies of Fusion Pores. *J. Membr. Biol.* **231**, 101–115 (2009).

46. Lin, D. H. & Hoelz, A. The Structure of the Nuclear Pore Complex (An Update). *Annu. Rev. Biochem.* **88**, 725–783 (2019).

47. Bochicchio, D. & Monticelli, L. Chapter Five - The Membrane Bending Modulus in Experiments and Simulations: A Puzzling Picture. in *Advances in Biomembranes and Lipid Self-Assembly* (eds. Iglič, A., Kulkarni, C. V. & Rappolt, M.) vol. 23 117–143 (Academic Press, 2016).

48. Torbati, M., Lele, T. P. & Agrawal, A. Ultradonut topology of the nuclear envelope. *Proc. Natl. Acad. Sci. U. S. A.* **113**, 11094–11099 (2016).

49. Gauthier, N. C., Masters, T. A. & Sheetz, M. P. Mechanical feedback between membrane tension and dynamics. *Trends Cell Biol.* **22**, 527–535 (2012).

50. Agrawal, A. & Lele, T. P. Mechanics of nuclear membranes. *J. Cell Sci.* **132**, jcs229245 (2019).

51. Matsuda, A. & Mofrad, M. R. K. On the nuclear pore complex and its emerging role in cellular mechanotransduction. *APL Bioeng.* **6**, 011504 (2022).

52. Schirmer, E. C., Florens, L., Guan, T., Yates, J. R. & Gerace, L. Nuclear Membrane Proteins with Potential Disease Links Found by Subtractive Proteomics. *Science* **301**, 1380–1382 (2003).

53. Akhtar, A. & Gasser, S. M. The nuclear envelope and transcriptional control. *Nat. Rev. Genet.* **8**, 507–517 (2007).

54. Dorner, D., Gotzmann, J. & Foisner, R. Nucleoplasmic lamins and their interaction partners, LAP2α, Rb, and BAF, in transcriptional regulation. *FEBS J.* **274**, 1362–1373 (2007).

55. Beiter, J. & Voth, G. A. Making the cut: Multiscale simulation of membrane remodeling. *Curr. Opin. Struct. Biol.* **87**, 102831 (2024).

56. Pezeshkian, W. & Marrink, S. J. Simulating realistic membrane shapes. *Curr. Opin. Cell Biol.* **71**, 103–111 (2021).

57. Pezeshkian, W., König, M., Marrink, S. J. & Ipsen, J. H. A Multi-Scale Approach to Membrane Remodeling Processes. *Front. Mol. Biosci.* **6**, (2019).

58. Evans, E., Heinrich, V., Ludwig, F. & Rawicz, W. Dynamic Tension Spectroscopy and Strength of Biomembranes. *Biophys. J.* **85**, 2342–2350 (2003).

59. Evans, E. & Smith, B. A. Kinetics of hole nucleation in biomembrane rupture. *New J. Phys.* **13**, 095010 (2011).

60. Lipowsky, R. *et al.* Elucidating the Morphology of the Endoplasmic Reticulum: Puzzles and Perspectives. *ACS Nano* **17**, 11957–11968 (2023).

61. Upadhyaya, A. & Sheetz, M. P. Tension in Tubulovesicular Networks of Golgi and Endoplasmic Reticulum Membranes. *Biophys. J.* **86**, 2923–2928 (2004).

62. Zucker, B., Golani, G. & Kozlov, M. M. Model for ring closure in ER tubular network dynamics. *Biophys. J.* **122**, 1974–1984 (2023).

63. Otsuka, S. *et al.* Postmitotic nuclear pore assembly proceeds by radial dilation of small membrane openings. *Nat. Struct. Mol. Biol.* **25**, 21–28 (2018).

64. Dasanna, A. K. & Fedosov, D. A. Mesoscopic modeling of membranes at cellular scale. *Eur. Phys. J. Spec. Top.* **233**, 3053–3071 (2024).

65. Duncan, A. L. & Pezeshkian, W. Mesoscale simulations: An indispensable approach to understand biomembranes. *Biophys. J.* **122**, 1883–1889 (2023).

66. Siggel, M., Kehl, S., Reuter, K., Köfinger, J. & Hummer, G. TriMem: A parallelized hybrid Monte Carlo software for efficient simulations of lipid membranes. *J. Chem. Phys.* **157**, 174801 (2022).

67. Physical mechanisms of ESCRT-III–driven cell division. https://www.pnas.org/doi/10.1073/pnas.2107763119.

68. Sadeghi, M. & Noé, F. Large-scale simulation of biomembranes incorporating realistic kinetics into coarse-grained models. *Nat. Commun.* **11**, 2951 (2020).

69. Davtyan, A., Simunovic, M. & Voth, G. A. The mesoscopic membrane with proteins (MesM-P) model. *J. Chem. Phys.* **147**, 044101 (2017).

70. Ayton, G. S., Blood, P. D. & Voth, G. A. Membrane Remodeling from N-BAR Domain Interactions: Insights from Multi-Scale Simulation. *Biophys. J.* **92**, 3595–3602 (2007).

71. Pezeshkian, W. & Ipsen, J. H. Creasing of flexible membranes at vanishing tension. *Phys. Rev. E* **103**, L041001 (2021).